Cardiovascular Engineering and Technology, Vol. 10, No. 2, June 2019 *(© 2019)* pp. 299–313
https://doi.org/10.1007/s13239-019-00411-8

Development of a Two-Way Coupled Eulerian–Lagrangian Computational Magnetic Nanoparticle Targeting Model for Pulsatile Flow in a Patient-Specific Diseased Left Carotid Bifurcation Artery

RODWARD L. HEWLIN JR.,[1,2] ASHLEY CIERO,[1] and JOHN P. KIZITO[3]

[1]Department of Engineering Technology & Construction Management (ETCM), University of North Carolina at Charlotte, Charlotte, NC, USA; [2]Center for Biomedical Engineering & Science (CBES), University of North Carolina at Charlotte, Charlotte, NC, USA; and [3]Department of Mechanical Engineering, North Carolina Agricultural & Technical State University, Greensboro, NC, USA

(Received 13 November 2018; accepted 26 March 2019; published online 29 March 2019)

Associate Editor Ajit P. Yoganathan oversaw the review of this article.

Abstract

Purpose—The aim of the present work is to present the development of a computational two-way coupled (*fluid and particle coupled*) magnetic nanoparticle targeting model to investigate the efficacy of magnetic drug targeting (MDT) in a patient-specific diseased left carotid bifurcation artery. MDT of therapeutic agents using multifunctional carrier particles has the potential to provide effective treatment of both cancer and cardiovascular disease by enabling a variety of localized treatment and diagnostic modalities while minimizing side effects.

Methods—A computational model is developed to analyze pulsatile blood flow, particle motion, and particle capture efficiency in a diseased left carotid bifurcation artery using the magnetic properties of magnetite (Fe_3O_4) and equations describing the magnetic forces acting on particles produced by an external cylindrical electromagnetic coil. A Eulerian–Lagrangian technique is adopted to resolve the hemodynamic flow and the motion of particles under the influence of a magnetic field ($B_r = 2T$). Particle diameter sizes of 20 nm–4 μm in diameter were considered.

Results—The computational simulations demonstrate that the greatest particle capture efficiency results for particle diameters within the micron range, specifically 4 μm in regions where flow separation and vortices are at a minimum. It was also determined that the capture efficiency of particles decreases substantially with particle diameter, especially in the superparamagnetic regime. Particles larger than 2 μm were targeted and captured at the desired location by the external magnetic field, and the largest capture efficiency observed was approximately 98%.

Conclusion—The simulation results presented in the present work have shown to yield favorable capture efficiencies for micron range particles and a potential for enhancing capture efficiency of superparamagnetic particles in smaller arteries and/or using magnetized implants such as cardiovascular stents. The present work presents results for justifying further investigation of MDT as a treatment technique for cardiovascular disease.

Keywords—Capture efficiency, Carotid artery, Diseased, Eulerian, Lagrangian, Magnetic drug targeting, Magnetite, Patient-specific, Pulsatile flow.

INTRODUCTION

Cardiovascular disease is the leading cause of death worldwide.[2] Medical drug delivery *via* the use of iron oxide magnetic nanoparticles as carrier vehicles for therapeutic agents under the influence of a magnetic field in cardiovascular flow has received much attention for the prospects of treatment processes for cancer and cardiovascular disease. This drug delivery scheme promises improvements in diagnosis and therapeutic treatments by increasing targeting efficacy while avoiding and/or minimizing systemic circulation which often causes added toxicity to healthy sites. However, despite ongoing research of cardiovascular flows and magnetic targeting as a potential candidate for medical drug delivery for cancer and cardiovascular disease, the fluid dynamics as well as the magnetic effects associated with MDT is poorly understood.

Address correspondence to Rodward L. Hewlin Jr., Department of Engineering Technology & Construction Management (ETCM), University of North Carolina at Charlotte, Charlotte, NC, USA. Electronic mail: rhewlin@uncc.edu

Targeting particles in cardiovascular flow is dependent upon the magnetic and hydrodynamic forces acting on particles.[1,19,20] As a result, the physical properties, magnetic field strength, and flow parameters such as drag force, wall shear stress, and vorticity have a major effect on effective particle targeting. Various experimental studies have been reported on characterizing the behavior of magnetic nanoparticles in research and clinical applications. One of the first clinical trials incorporated permanent external magnets to target tumors in the body *via* chemotherapeutic removal techniques.[27] In the efforts of targeting locations deeper in the body, the use of magnetic stents[2,7,13,37] and implants[16,25,30] have been investigated and reported. Forbes *et al.*[14] proposed a technique that involves exposing a magnetizable stent to an external magnetic field to target particles for potential cell therapy techniques. Two independent magnetic field sources are used to allow deep penetration within the subject: one is an external high gradient magnetic field to attract the magnetic drug carriers to the stent, the other is the magnetic field induced by the magnetized stent which attract particles to regions of interest. This reported approach can not only improve the capture efficiency of particles in the injury region of interest, but present a potential solution to one of the major problems caused by in stent-restenosis.[17] This is because particles can continuously and quantitatively provide anti-proliferative agents. Chorny *et al.*[9,11,12,32] and other researchers[10] later conducted studies to verify and improve this method.

A small number of numerical studies have also been carried out to investigate the behavior of magnetic nanoparticles in physiological flow under the influence of a magnetic field.[3,4,22,33] Finite element methods (FEMs) have been widely used to investigate the motion of particles under different physical conditions.[26,38] Wong *et al.*[40] applied FEM simulations of magnetic particle inspection to analyze the magnetic field around a defect. A few studies have been reported that implemented simulation models based on a finite volume approach to solve the Navier–Stokes equations and a refined discrete particle motion model to solve the equations of motion of particles due to an external magnetic field.[4,22] These studies have reported that the simulation results indicate a significant potential for the treatment of atherosclerosis. Based on studies of previous researchers, the targeting method of magnetic nanoparticles still needs to be improved due to its limited capture efficiency.

The present work presents the development of a magnetic nanoparticle tracking model which was used to investigate the transport and targeting efficiency of magnetite (Fe_3O_4) nanoparticles dispersed in a patient-specific diseased left carotid bifurcation artery and targeted by an external magnetic field. All the simulations are performed using ANSYS Fluent™ 19. The blood flow in the arterial vessel is modelled as non-Newtonian, incompressible, laminar, and transient. The forces that have effects on the particles are viscous drag, buoyancy, and magnetic forces. A cylindrical electromagnetic coil is modelled as the source of the external magnetic field. The influence of blood flow and magnetic field strength on particle capture efficiency is investigated.

THEORETICAL FORMULATION AND NUMERICAL METHODS

Blood Flow

All blood flow and particle tracking analyses were conducted in ANSYS Fluent™ 19. For blood flow simulations, the continuity and three-dimensional Navier–Stokes equations describing the pulsatile flow of blood as an incompressible fluid is implemented and numerically solved in a finite volume formulation:

$$\nabla \cdot u = 0 \tag{1}$$

$$\rho\left(\frac{\partial u}{\partial t} + u(u \cdot \nabla)\right) = -\nabla p + \nabla \cdot (\mu \nabla u) \tag{2}$$

where u is the three-dimensional velocity vector, ρ is the density of blood, p is pressure, and μ is the dynamic viscosity. The rheology of blood is also considered as described by the non-Newtonian Carreau model:

$$\mu(\dot{\gamma}) = \mu_\infty + (\mu_0 - \mu_\infty)(1 + (\lambda\dot{\gamma})^2)^{\frac{n-1}{2}} \tag{3}$$

where $\dot{\gamma}$ is the strain rate, μ_∞ (0.0035 kg/m s) is the infinite viscosity, μ_0 (0.056 kg/m s) is the zero-shear viscosity, λ (3.313) is the time constant, and n (0.3568) is the power law index. A patient-specific left carotid bifurcation artery geometry was used for all blood flow and particle simulations and was obtained from the Charite' Clinical Research Hospital in Berlin Germany. The geometry was uploaded as a point cloud image and reconstructed in Solidworks using a 3-D plane construction, surface spline generation, and boundary boss uniting methodology. More details on

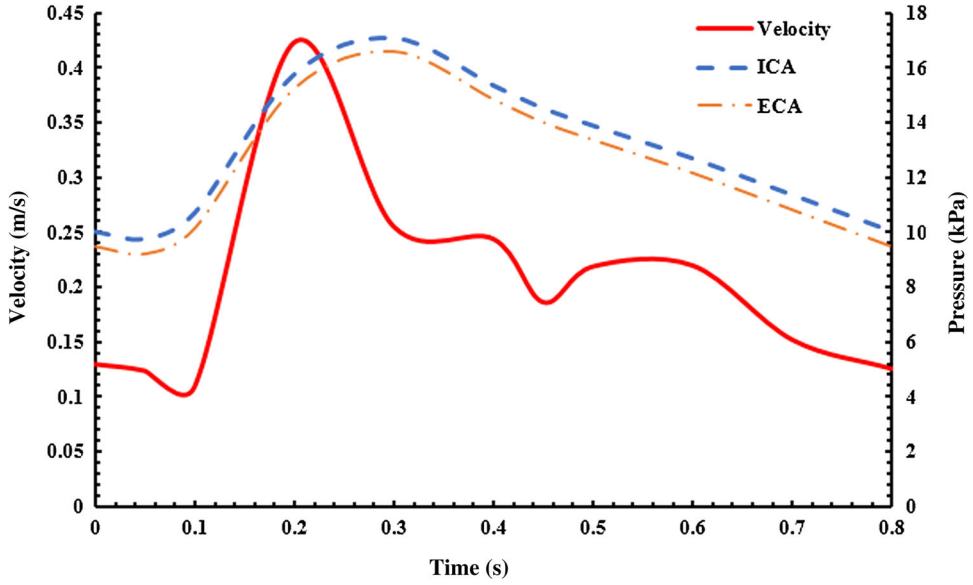

FIGURE 1. Plot of unsteady inlet velocity waveform and Windkessel outlet waveforms.

this methodology can be found in Refs. 23 and 24 A piecewise unsteady velocity waveform is implemented at the inlet of the model as shown in Fig. 1 and Eq. (4). The unsteady inlet velocity is modeled as fully developed as shown in Eq. (5). The walls of the arterial vessel are modeled as a rigid vessel with the no slip condition applied at the boundary.

TABLE 1. Resistance and capacitance values used for the Windkessel boundary conditions. Values obtained from Gharahi *et al.*[18]

	R_d (Pa s/m^3)	C (m^3/Pa)	R_p (Pa s/m^3)
ICA	1.11×10^6	4.20×10^{-13}	8.15×10^{11}
ECA	2.27×10^6	2.27×10^{-13}	4.07×10^{12}

$$\bar{u}(t) = \begin{cases} 83.33t^3 - 12.50t^2 + 0.21667t + 0.13 & 0\ s \le t \le 0.15\ s \\ 7517.12t^4 - 5688.27t^3 + 1529.70t^2 - 169.61t + 6.6462 & 0.15\ s \le t \le 0.24\ s \\ -96.923t^3 + 100.30t^2 - 34.425t + 4.1629 & 0.24\ s \le t \le 0.42\ s \\ 58.291t^2 - 5235.7t + 1193 & 0.42\ s \le t \le 0.47\ s \\ 18.835t^3 - 36.960t^2 + 23.427t - 4.60 & 0.47\ s \le t < 0.80\ s \end{cases} \quad (4)$$

$$u(y,t) = 2\bar{u}(t)\left[1 - \left(\frac{y}{R}\right)^2\right] \quad (5)$$

The outlet pressures of the external carotid artery (ECA) and internal carotid artery (ICA) are modelled using Windkessel boundary conditions. The Windkessel boundary conditions are expressed through an ordinary differential equation (ODE) similar to the relation between voltage and current in electrical circuits. The ODE used for blood flow and particle simulations in the present work is shown in Eq. (6), where R_p is proximal resistance for large arteries and arterioles, R_d is the distal resistant for simulating small arterioles and capillaries, C is vessel capacitance for large arteries and arterioles, $i(t)$ represents the flow rate, and $p(t)$ is the time dependent pressure. Table 1 list the values used to model the Windkessel boundary conditions for the present work.

$$\left(1 + \frac{R_p}{R_d}\right) i(t) + CR_d \frac{di(t)}{dt} = \frac{p(t)}{R_d} + C\frac{dp(t)}{dt} \quad (6)$$

Wall shear stress (WSS) and vorticity values are predicted on the fluid domain surfaces that represent the interface boundary between the fluid and the neighboring tissue. The equations used to calculate these hemodynamic parameters are shown below. Wall shear stress is calculated using Eq. (7) and vorticity is calculated using Eq. (8). Vorticity ω in Eq. (8) is evaluated by $\varpi \equiv \nabla \times u$, where u is the velocity.

$$\tau_{yx} = \tau_{xy} = \mu\left(\frac{\partial u}{\partial y} + \frac{\partial v}{\partial x}\right) \quad (7)$$

$$\frac{D\varpi}{Dt} = (\varpi \cdot \nabla)u + \nu\nabla^2\varpi \tag{8}$$

Particle Force Balance

The physics describing the transport of magnetic nanoparticles in the cardiovascular system is governed by various factors: (1) the magnetic force produced by the external magnet, (2) viscous drag, (3) unsteady effects due to the driving pressure wave, (4) particle kinematics (*Brownian motion*), and (5) the interaction between the fluid and particles. In the present work, our model incorporates the dominant magnetic and viscous forces and the particle/blood interaction through an integrated force balance. This is done *via* deriving the magnetic force exerted on a cluster (*parcel*) of particles. Each particle has a radius R_{mp} and a spherical volume V_{mp}. The magnetic force exerted on the particles is derived from a dipole moment approach in which the particle is replaced by an equivalent point dipole which is focused at the center. The magnetic force computed on a parcel of particles in a non-conducting medium described as:

$$F_m = \frac{4}{3}\pi R_{mp}^3 \mu_0 \frac{3\chi_{mp}}{(\chi_{mp}+3)}(H \cdot \nabla)H, \tag{9}$$

where H is the applied magnetic field intensity at the center of the parcel, χ_{mp} is the magnetic susceptibility (3.1) and μ_0 ($4\pi \times 10^{-7}$ N A^{-2}) is the permeability in air.[15] The derivation of the magnetic force incorporates the assumption that blood is a non-magnetic medium with permeability. The magnetic field in the present work is modelled as a cylindrical electromagnet of radius R_{mag} that is positioned a distance d orthogonal to the axial flow field as shown in Fig. 2. The magnetic field is described as:

$$H_x(x,y) = \frac{M_s R_{mag}^2}{2}\left(\frac{(x+d)^2 - y^2}{((x+d)^2+y^2)^2}\right) \tag{10}$$

and

$$H_y(x,y) = \frac{M_s R_{mag}^2}{2}\left(\frac{2(x+d)y}{((x+d)^2+y^2)^2}\right) \tag{11}$$

Equations (10) and (11) are substituted into Eq. (9) to determine the magnetic force components as described below in Eqs. (12) and (13):

$$F_{mx}(x,y) = \frac{4}{3}\pi R_{mp}^3 \mu_0 \frac{3\chi_{mp}}{(\chi_{mp}+3)} \times \left[H_x(x,y)\frac{\partial H_x(x,y)}{\partial x} + H_x(x,y)\frac{\partial H_x(x,y)}{\partial y}\right] \tag{12}$$

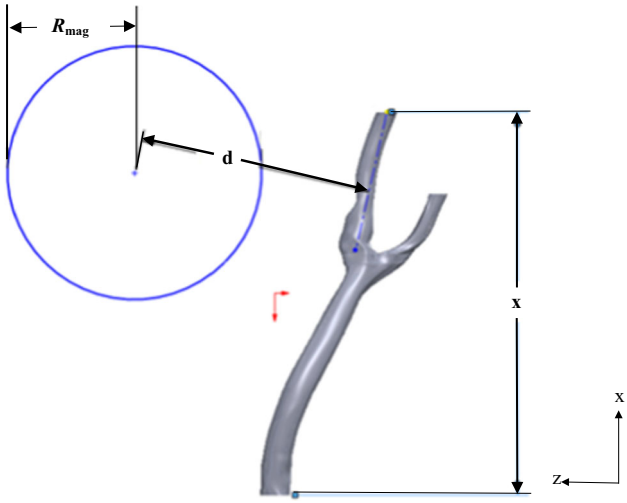

FIGURE 2. Schematic representation of the circular electromagnet of radius "Rmag" distanced "d" from the centerline of the ICA.

and

$$F_{my}(x,y) = \frac{4}{3}\pi R_{mp}^3 \mu_0 \frac{3\chi_{mp}}{(\chi_{mp}+3)} \times \left[H_y(x,y)\frac{\partial H_y(x,y)}{\partial x} + H_y(x,y)\frac{\partial H_y(x,y)}{\partial y}\right] \tag{13}$$

Equations (12) and (13) may be simplified *via* the differential product rule to yield the following magnetic field force components:

$$F_{mx} = \frac{-3\pi\mu_0 R_{mp}^3 \chi_{mp} M_s^2 R_{mag}^4}{\chi_{mp}+3}\frac{(x+d)}{2\left((x+d)^2+y^2\right)^3} \tag{14}$$

and

$$F_{my} = -\frac{3\pi\mu_0 R_{mp}^3 \chi_{mp} M_s^2 R_{mag}^4}{\chi_{mp}+3}\frac{y}{2\left((x+d)^2+y^2\right)^3} \tag{15}$$

The derived model describes the targeting of a parcel of particles embedded with magnetite (Fe_3O_4) particles as described by Takayasu *et al.*[36] and Furlani and Furlani.[15] Magnetite nanoparticles are biocompatible and have a density $\rho_p = 5230$ kg/m^3.[28] For the magnetic field source, a 6 cm in diameter (radius 3 cm) electromagnet, with a magnetization of $M_s = 1.5915 \times 10^6$ A/m (remanence $B_r = 2.0T$) is modelled. The surface of the magnet is positioned 2.4 cm from the centerline axis of ICA branch of the carotid bifurcation.

Particle Trajectory Model

A discrete phase model (DPM) was implemented in the present work. This approach follows the Euler–Lagrange approach. The interaction with continuous phase option was enabled in Fluent to allow the discrete phase (particle clusters) to exchange mass, momentum, and/or energy with the continuous phase (blood). The trajectory of the particles is predicted by integrating the force balance on the particle cluster, which is written in a Lagrangian reference frame. The force balance equates the particle cluster inertia with the forces acting on the particles and can be expressed as:

$$\frac{\mathrm{d}u_\mathrm{p}}{\mathrm{d}t} = F_\mathrm{D}(u - u_\mathrm{p}) + \frac{g_\mathrm{x}(\rho_\mathrm{p} - \rho)}{\rho_\mathrm{p}} + F_\mathrm{bi} + F_\mathrm{x} \tag{16}$$

where u is the fluid velocity, u_p is the particle velocity, ρ is the fluid density, ρ_p is the particle density, F_bi is the Brownian force acceleration term, F_x is the body force acceleration term, d_p is the particle diameter, and $F_\mathrm{D}(u - u_\mathrm{p})$ is the drag force per unit mass and is written as:

$$F_\mathrm{D} = \frac{18\mu}{\rho_\mathrm{p} d_\mathrm{p}^2}\frac{C_\mathrm{D}\mathrm{Re}}{24} \tag{17}$$

The relative Reynolds number, "Re" is defined as:

$$\mathrm{Re} = \frac{\rho d_\mathrm{p}|u_\mathrm{p} - u|}{\mu} \tag{18}$$

the drag coefficient, "C_D" is defined as:

$$C_\mathrm{D} = \mathrm{a}_1 + \frac{\mathrm{a}_2^2}{\mathrm{Re}} + \frac{\mathrm{a}_3^3}{\mathrm{Re}^2} \tag{19}$$

where a_1, a_2, and a_3 are constants that apply for smooth particles using the spherical drag law and apply over a range of Reynolds numbers as reported by Morsi and Alexander.[29] For the present work, when substituting the appropriate constants, the drag coefficient takes the following form for micron sized particles:

$$C_\mathrm{D} = \frac{24}{\mathrm{Re}}\left(1 + b_1\mathrm{Re}^{b_2}\right) + \frac{b_3\mathrm{Re}}{b_4 + \mathrm{Re}} \tag{20}$$

where

$$b_1 = \exp(2.3288 - 6.4581\phi + 2.4486\phi^2)$$
$$b_2 = 0.0964 + 0.5565\phi$$
$$b_3 = \exp(4.905 - 13.8944\phi + 18.4222\phi^2 - 10.2599\phi^3)$$
$$b_4 = \exp(1.4681 + 12.2584\phi - 20.7322\phi^2 + 15.8855\phi^3)$$

which is adapted from Haider and Levenspeil.[21] The shape factor, "ϕ" is defined as:

$$\phi = \frac{s}{S} \tag{21}$$

where s is the surface area of a sphere having the same volume as the particle, and S is the actual area of the particle. The shape factor cannot exceed a value of 1. For superparamagnetic particles, a form of Stokes drag law is used.[31] In this case, the drag force on a particle per unit mass is defined as:

$$F_\mathrm{D} = \frac{18\mu}{d_\mathrm{p}^2\rho_\mathrm{p}C_\mathrm{e}} \tag{22}$$

where the Cunningham correction factor C_e is described as:

$$C_\mathrm{e} = 1 + \frac{2\lambda}{d_E}\left(1.257 + 0.4e^{-(1.1d_\mathrm{p}/2\lambda)}\right) \tag{23}$$

and λ is the molecular mean free path. For superparamagnetic particles, the effects of Brownian motion are included. The components of the Brownian force are modeled as a Gaussian white noise process with spectral density given by $S_{n,ij}$.

$$S_{n,ij} = S_0\delta_{ij} \tag{24}$$

where δ_{ij} is the Kronecker delta function and modelled as:

$$S_0 = \frac{216\nu k_\mathrm{B}T}{\pi^2\rho d_\mathrm{p}^5\left(\frac{\rho_\mathrm{p}}{\rho}\right)C_\mathrm{e}} \tag{25}$$

T is the absolute temperature of the fluid (*taken as body temperature*), ν is the kinematic viscosity, and k_B is the Boltzmann constant. The Brownian force per unit mass component is described as:

$$F_\mathrm{bi} = \zeta_i\sqrt{\frac{\pi S_0}{\Delta t}} \tag{26}$$

where ζ_i is the zero-mean unit-variance-independent Gaussian random number.

Particle Capture Efficiency

One of the most reported challenges for MDT is the capability of targeting and capturing particles *via* producing a magnetic force to overcome the drag force acting on particles due to the inlet pressure wave. As a result, capture efficiency is a major parameter of interest in the present work. Capture efficiency describes the effectiveness of targeting particles under the influence of a magnetic field. The capture efficiency for the magnetized section of the artery is defined as the ratio of the number of injected particle parcels to the number of particle parcels leaving the magnetized region:

$$\eta_c = \frac{N_{np,\,out}}{N_{np,\,in}} \times 100\% \quad (27)$$

In the present work, Eq. (27) is evaluated *via* imposing a reflective boundary condition at the wall of the magnetized section [*region of interest (ROI)*]. Previous studies that have utilized a trapped boundary condition as opposed to a reflective boundary condition.[5] A trapped boundary condition cancels the trajectory mapping of particle trajectories as opposed to continuously monitoring the trajectory if the particles move from the current position in a future time step. Additionally, an escape boundary condition is imposed at the outlets which allow particles to escape (*exit*) the outlets. The capture efficiency is determined *via* comparing the number of escaped particle parcels $N_{np,\,out}$ to the number of injected particle parcels $N_{np,\,in}$ as described in Eq. (27).

NUMERICAL METHODS

The pulsatile flow of blood and particle tracking was calculated *via* ANSYS Fluent^{TM} 19. The magnitude of the magnetic force components is substituted into the accelerated body force term in Eq. (16). User defined functions were written for the pulsatile velocity waveform and the magnetic force generated by the magnetic field. The user defined functions were compiled in the ANSYS Fluent platform for simultaneous flow and particle trajectory calculations. The Navier–Stokes equations were solved implicitly using a quadratic upwind discretization scheme (QUICK) for nonlinear terms. The integrated force balance described in Eq. (16) was numerically integrated using a sixth order Runge–Kutta scheme for instances where the left side of the equation was significant, and a Euler scheme otherwise. A two-way fluid-particle coupling method is implemented in Fluent to predict the effect of the discrete phase on the continuum. This method solves the discrete and continuous phase equations until the solutions of both phases have stopped changing.

The flow domain was discretized into a large number of tetrahedral computational cells. The arterial model was tested for three different mesh grid densities, i.e., 274, 548, and 1096 cells in the cross-sectional flow area. The time-averaged absolute difference in centerline axial velocity between the coarse and fine cross-sectional mesh was 2.2 mm/s, and that between fine and finer one was only 1 mm/s, which was very small relative to the mean centerline axial velocity value of 105 mm/s.

The mesh scheme that contained 548 cells per cross-section, i.e., 230,608 for the whole arterial mesh as shown in Fig. 3 and evaluated over 80 time steps per cycle provided the best grid result for independency and stability in solutions within a satisfactory CPU time.

RESULTS

Blood Flow Results

The ability to target particles in the cardiovascular system is dependent on the capability of overcoming the hydrodynamic drag produced by cardiovascular flow. Also, it is evident that cardiovascular flow is highly unsteady, which has a huge effect on hemodynamic parameters. The flow characteristic profile inside the stenosed carotid bifurcation artery is shown in Fig. 4 for both systole and diastole during cycle 3 of the cardiac flow waveform. Contours of axial velocities have been plotted along eight sliced planes normal to the direction of flow. Flow streamlines representing the trajectory of finite fluid particles are tracked and superimposed on the transparent mesh and the axial velocity contours. As depicted in slice 3 of both diastole and systole, a Womersley flow profile is established upstream of the sinus bulb region of slice 3 and continues throughout the artery for both cases in the cardiac cycle observed. During diastole the flow is

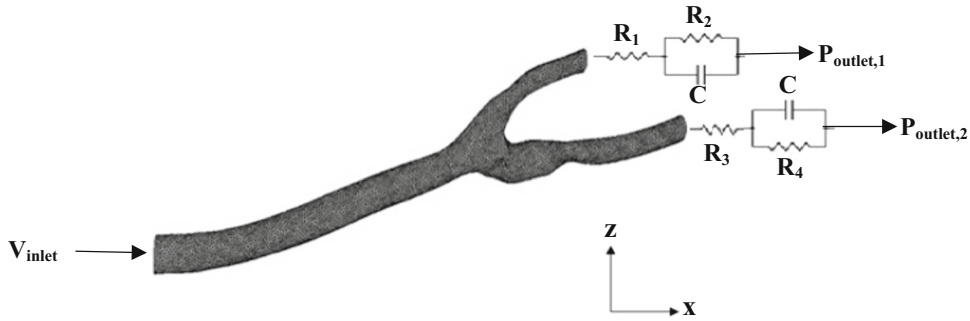

FIGURE 3. Top view of the arterial computational mesh.

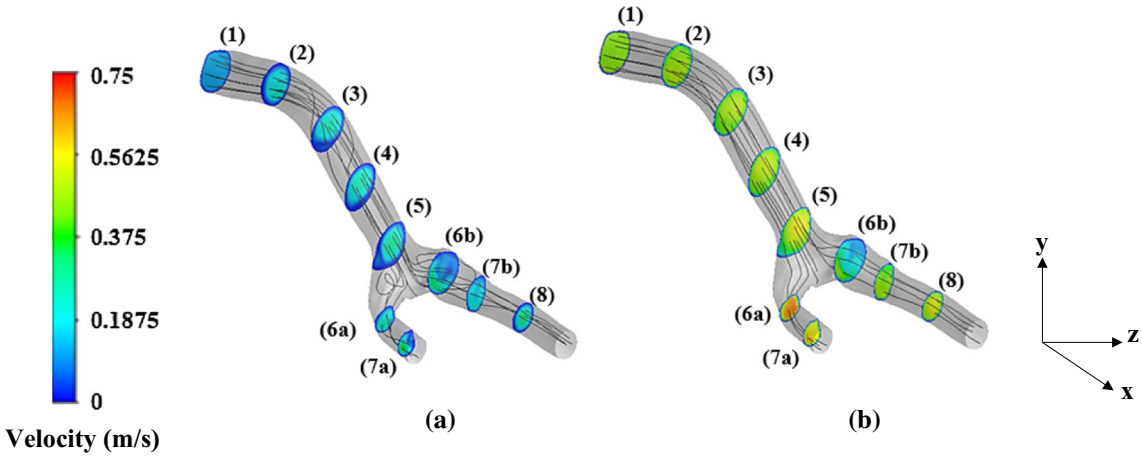

FIGURE 4. Contour plots of velocity and streamline traces of blood flow during (a) diastole and (b) systole (3rd cardiac cycle).

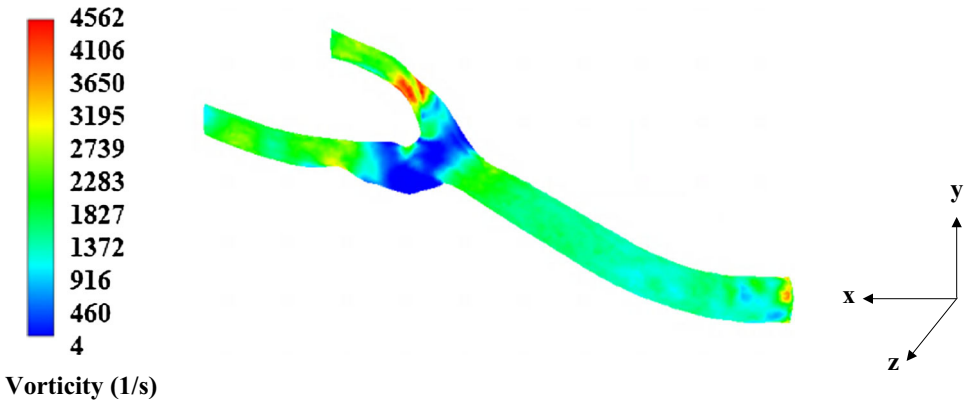

FIGURE 5. Contour of flow vorticity at systole.

highly skewed towards the wall as shown in each axial velocity contour. The streamlines are also disorganized in the common carotid artery (CCA) region and show areas of flow separations and secondary flow upstream of the internal and external carotid artery (ICA and ECA). Similar findings have also been reported, whereby such skewed flow structure is primarily caused by the misalignment of the mean axis of the artery, curvature of the lumen, unsteady centrifugal forces caused by the sudden decrease and increase in flow velocity.[6,8,39]

The asymmetric flow pattern within the stenosed carotid artery plainly depicts strong unsteadiness (*not to be confused with turbulence as the Re = 545*) downstream of the sinus, while remaining flow dampens upstream of the sinus region. During diastole, fewer velocity profiles appear to have a Womersley profile and the streamlines are much more organized. This is believed to be due to the large momentum increase of fluid motion from systole to diastole in which the flow has achieved maximum flow. The sinus bulb region remains to have a Womersley profile which indicates that possibly some recirculating flow occurs in this region. A more conclusive examination can be predicted from a plot of the vorticity fields as shown in Fig. 5.

As shown in Fig. 5, from the bifurcation region to both the ICA and ECA, the flow changes significantly and becomes more chaotic with pronounced vortical coherent structures and strong central vortex threading being formed through the stenosed regions of both branches. These unsteady affects also effect WSS as shown in Fig. 6. The average range of WSS in the carotid artery is 1–12 Pa,[35,41] whereas in the present work the highest WSS occurs around 18.93 Pa at the stenosed region, indicating high near wall forces. The break-down of vortex structure in the post-stenotic region can also be observed. Flow separating areas that produce chaotic flow present huge barriers for particle targeting and capture. Moreover, the likely hood of particles sticking to the wall and remaining to the wall are highly unlikely without the presence of a magnetic field and during weak magnetic fields

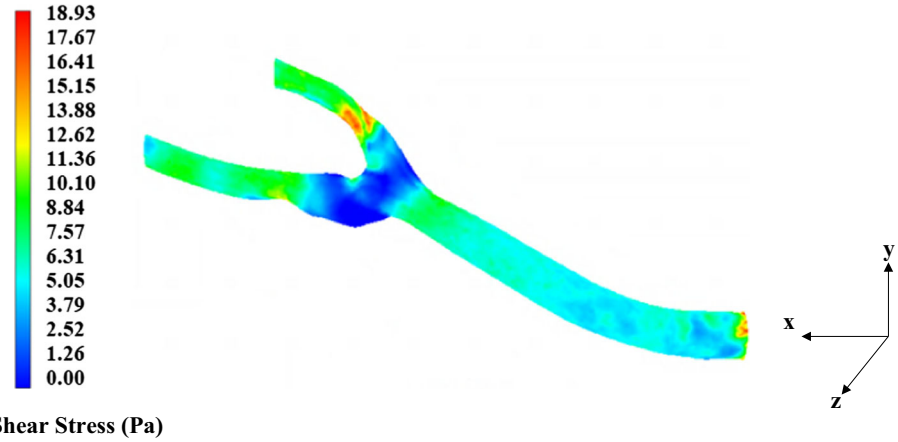

FIGURE 6. Wall shear stress contours at systole.

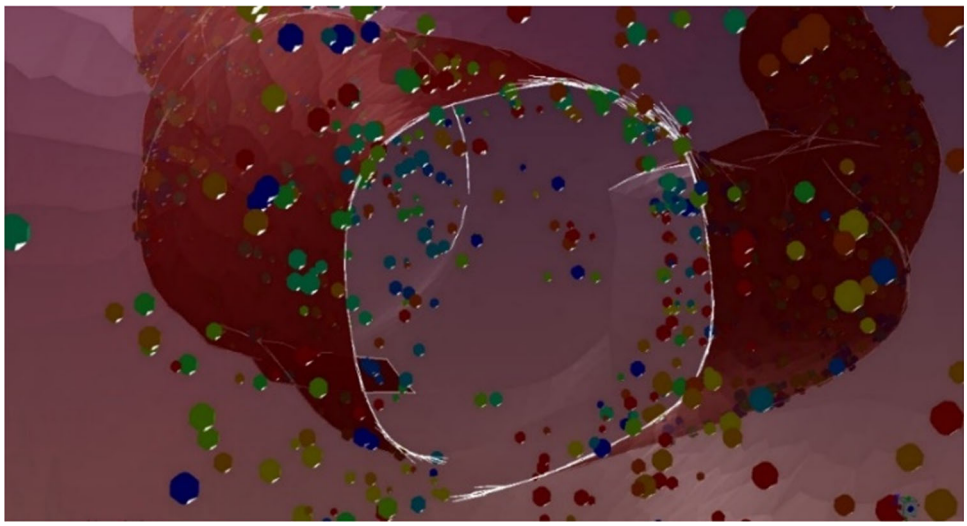

FIGURE 7. Interior view of dispersed particles inside the carotid bifurcation artery downstream of the bifurcation point and sinus bulb. The red tinted transparent wall is the artery wall.

($B_r > 1T$). In this case, the magnitude of hydrodynamic drag should be taken into consideration.

In the present work, particles with diameters ranging from 20 nm to 4 μm are uniformly injected into the flow through the inlet and subjected to the external magnetic field. The calculated drag forces that occur on particles ranging from 20 nm to 4 μm are of the range 0.025–12.48 pN. This indicates that a magnetic force must be generated higher than 12.48 pN to overcome the hydrodynamic drag.

Particle Flow and Capture Results

Pulsatile blood flow simulations with a periodic inlet velocity boundary condition were performed in which the particles were uniformly injected at the inlet face at time increments of 1/100th of the flow over a total time of 3.2 s. Over a time of 3.2 s, a homogeneous mixture of 73,184 magnetite particles were uniformly injected into the artery from the inlet. Figure 7 shows an interior view of the injected particles inside the carotid bifurcation artery downstream of the bifurcation point with the magnet turned off. The particles are colored by size and are scaled by 100 times the actual diameters.

The magnitude of the magnetic field strength within the flow field for cases when the magnet is turned on is shown in Fig. 8. The average magnetic field strength within the ROI site, specifically the sinus bulb and stenosed region (*upstream and downstream*) is approximately 0.571T. The magnitude of the force field generated by the magnetic field for 4 μm diameter particles dispersed in the flow field is shown in Fig. 9. The average force within the ROI site, specifically the sinus bulb and stenosed region is approximately 12.4 pN.

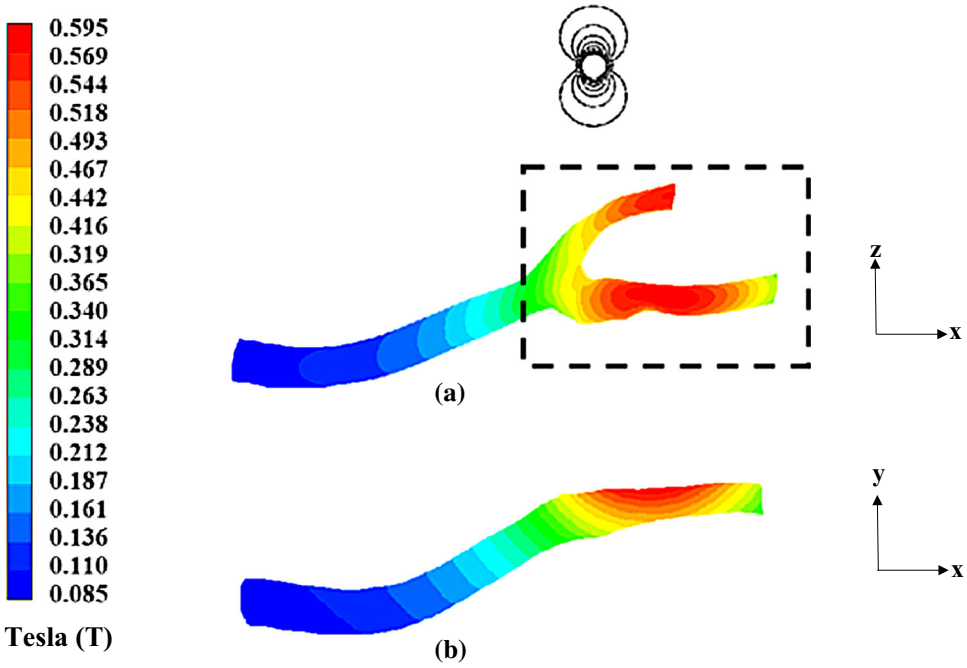

FIGURE 8. Contour of the arterial magnetic field strength at B_r= 2.0*T*: (a) top view and (b) bottom view generated in ANSYS Fluent. The black circle represents the magnet and the dashed line represents the region of interest (ROI).

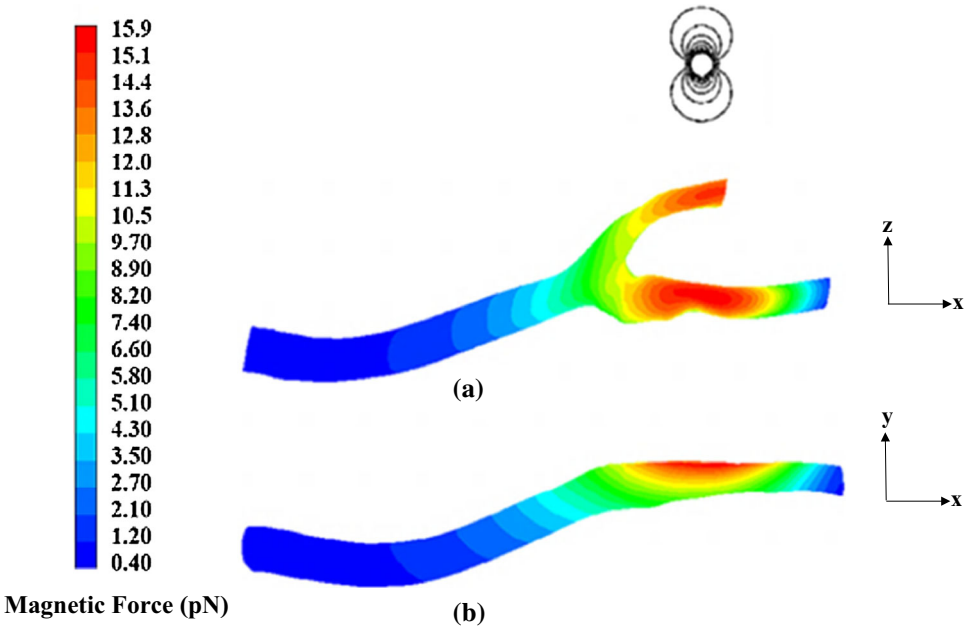

FIGURE 9. Contour of the magnetic pulling force *(towards the magnet)* exerted on 4 μm diameter particles at B_r= 2.0*T*: (a) top view and (b) bottom view generated in ANSYS Fluent. The black circle represents the magnet and the dashed line represents the region of interest (ROI).

A comparison analysis was conducted to illustrate the particle capture behavior for a normal artery vs. a diseased artery case. The same artery mentioned earlier was modified whereby the stenosis was removed to create an unrestricted flow boundary along the axial direction of where the stenosis was originally. This model is referred to as the normal artery, whereby the artery with the stenosis is referred to as the diseased artery. For both cases, particles were injected through the inlet face of the artery over a total time of 0.8 s with the magnet turned off. After 0.8 s, the magnet was turned on and simulations were ran over a total time of

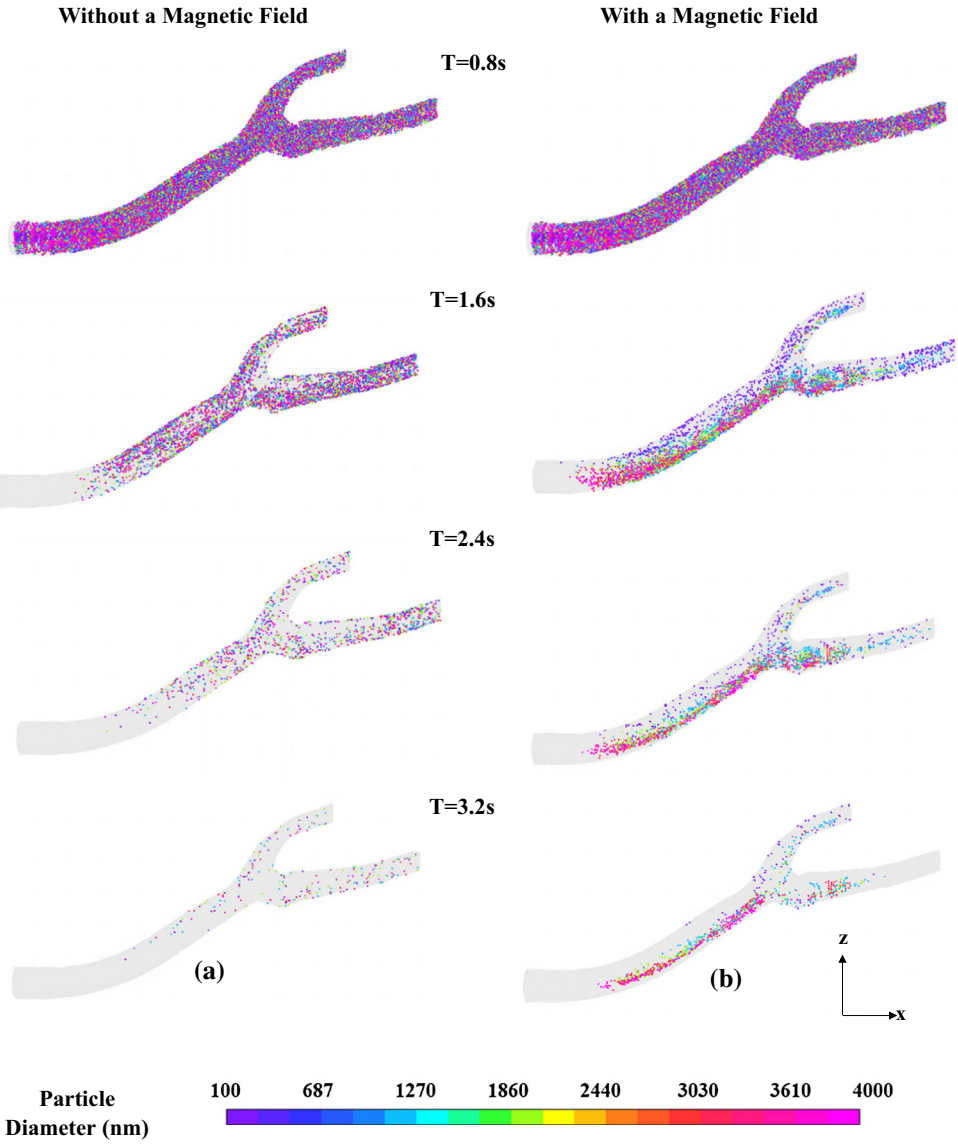

FIGURE 10. Particle distribution in the normal carotid artery at different time instances: (a) without a magnetic field and (b) with a magnetic field turned on at 0.8 s and for the duration of the tracking.

3.2 s. Figure 10 shows a top view (*view from the bottom of the magnet facing the artery*) of the particles dispersed in the normal artery during studies in which the magnet is turned off and for a case in which the magnet is turned on. Figure 11 also shows the same scenario for the diseased artery case.

For both the normal and diseased artery cases, during the time when the magnet is turned off, the particles are injected into the artery and flow throughout the artery due to the viscous drag force produced by the driving pressure wave as shown in both Figs. 10a and 11a. The particles follow the flow streamlines as their inertia is negligible compared to the viscous drag. As shown in both Figs. 10a and 11a, over a total time of 3.2 s, the majority of particles have exited the artery and only a few particles are found to adhere to the vessel walls due to the no slip condition. When the magnet is turned on, as shown in both Figs. 10b and 11b, the particles are found to be influenced appreciably by the magnetic force. For both the normal and diseased artery cases, the particles are shown to be attracted to the top portion of the vessel wall where they can exchange medical drugs with the arterial wall. For the diseased case however, the particles are shown to be skewed towards the top edge of the vessel wall. This phenomena is illustrated in Fig. 12.

As mentioned previously, the flow is axisymmetric in nature and the magnetic arrangement does not show angular or axial symmetry. For both cases, the

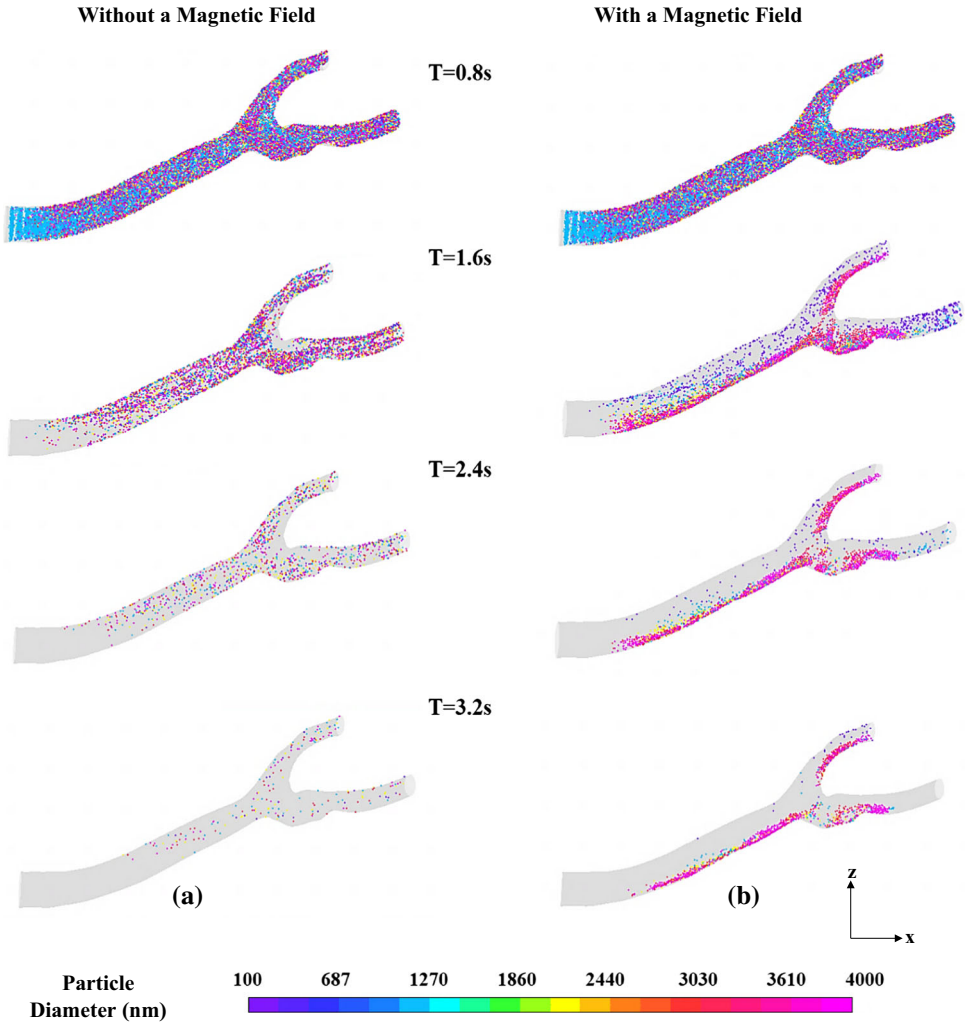

FIGURE 11. Particle distribution in the diseased carotid artery at different time instances: (a) without a magnetic field and (b) with a magnetic field turned on at 0.8 s and for the duration of the tracking.

majority of particles tend to be attracted to regions where recirculation is low. For the normal artery case, particle dispersion and capture appear to be balanced (equal) on both the ICA and ECA as compared to the diseased case at time 1.6 s in Fig. 10b. This is believed to be attributed to the fact that the lack of a stenosis on the ICA branch promotes smoother flow and equalized velocity distributions on both branches which allow a more balanced transport of particles on both branches. This phenomena also encourages the capture of smaller micronsized particles as shown in Fig. 10b for time 3.2 s.

For the diseased artery case, no particles are captured near the inner edge of the stenosed region. The inner edge of the stenosed region is a high recirculation zone and area where the Venturi effect causes a significant increase in velocity and makes particle capture difficult. However, when considering the capture efficiency in terms of particle diameter, a significant fraction of the captured particles are 4 μm in diameter. Similar results have been reported in previous studies.[5,28] This deems to be a positive result when considering *ex vivo* applications for MDT to large arterial sections. The overall capture efficiency of the homogeneous dispersion was found to be 77% for the diseased artery case. The overall capture efficiency of the homgenous dispersion for the normal artery case was 68%. In comparison, the normal artery allows more particles to escape overtime as compared to the diseased case due to the lack of a stenosis. For the diseased case, a capture efficiency quantitative analysis was conducted for homogenous dispersions of particle diameters ranging from the superparamagnetic region to 4 μm as shown in Fig. 13.

Figure 13 shows the calculation result for MDT capture efficiency as a function of particle diameter and varying magnetic field strength. The first observation is that the best capture efficiency results at

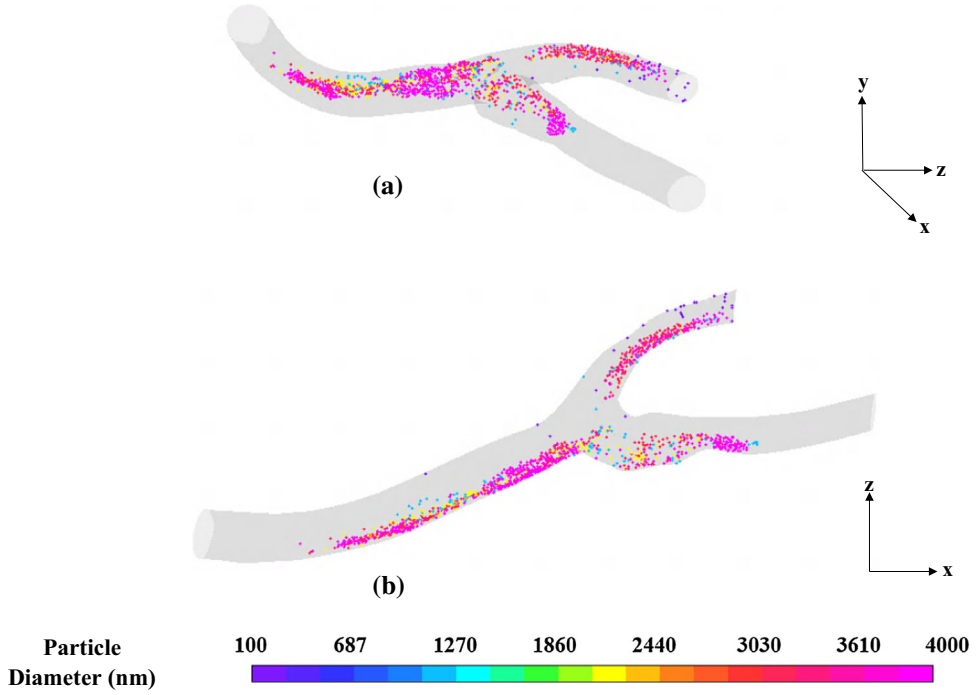

FIGURE 12. Particle distribution of captured particles in the diseased carotid artery at 4 s (B_r= 2*T*): (a) isometric view and (b) top view.

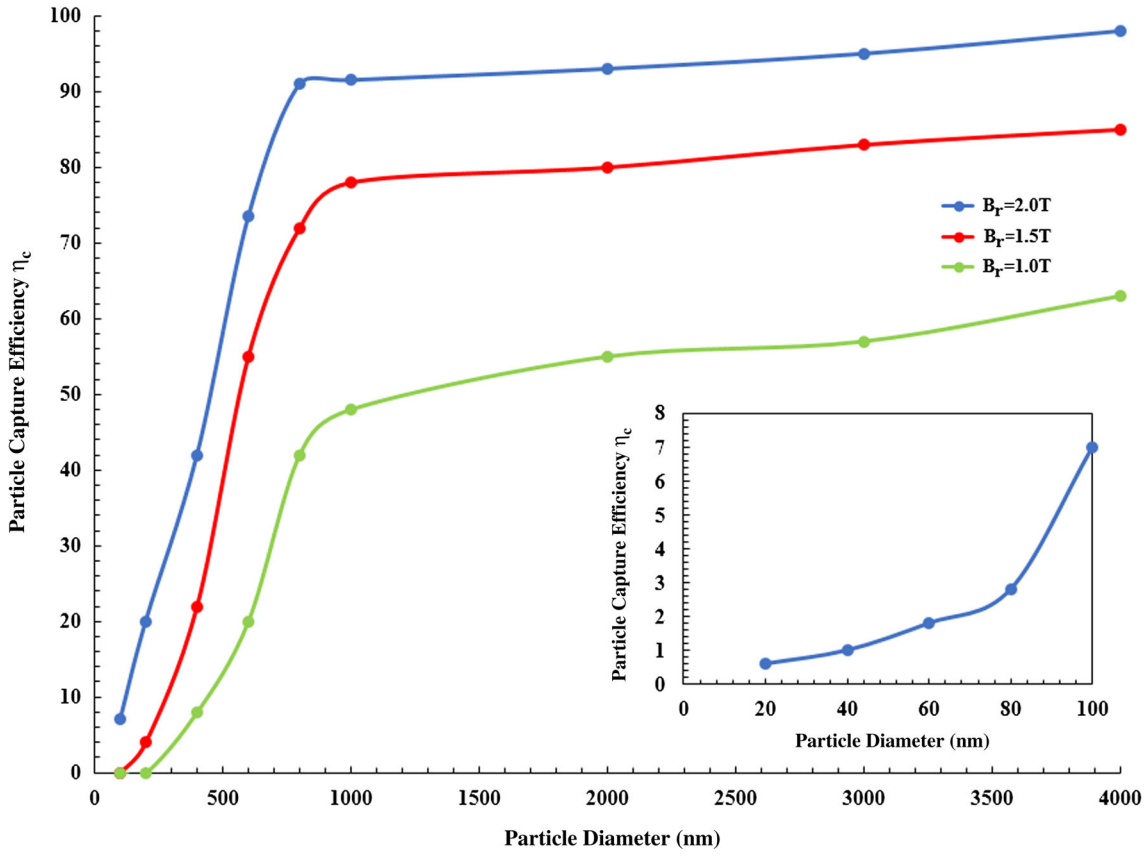

FIGURE 13. Plot of capture efficiency as a function of particle diameter and varying magnetic field strength in the diseased carotid artery. The inset shows the efficiency of MDT in the superparamagnetic regime at B_r= 2*T*.

$B_r = 2.0T$ as compared to lower magnetic field strengths. The second observation is that the larger diameter particles (micron sized particles) have better cumulative capture efficiency and targeting potential compared to smaller diameter particles (superparamagnetic particles). For the best capture efficiency case which occurs at $B_r = 2.0T$, high capture efficiencies of 92–98% were observed for particles larger than 1 μm in diameter. For particles with diameters ranging from 500 to 800 nm, capture efficiencies of 60–91% were observed. For smaller particles ranging from the superparamagnetic regime to 400 nm, capture efficiences of 0.5–30% was observed. As reported in previous studies, for *in vivo* applications and depending on the medical injection location, large particles ($D > 200$ nm) may be quickly eliminated by the reticuloendothelial system of the spleen and liver during continuous circulation in the cardiovascular system.[28,34] Smaller particles (10–200 nm) in diameter have been reported to be optimal for *in vivo* MDT as they can escape renal clearance, whereas the large particles are eliminated.

It is worth mentioning that the smaller diameter particles will flow past the magnetized region of interest again as they circulate continuously in the bloodstream for an *in vivo* case. The overall capture efficiency of smaller particles may potentially increase during an *in vivo* case through many passes, contrary to what is shown in Fig. 13.

CONCLUSION

Three dimensional modelling of pulsatile blood flow, particle motion, and particle tracking was performed in a patient-specific diseased left carotid bifurcation artery using the magnetic properties of magnetite (Fe_3O_4) and equations describing the forces acting on particles produced by an external cylindrical electromagnetic coil. A two-way coupled (*fluid and particle coupled*) Eulerian–Lagrangian technique was adopted and implemented to resolve the hemodynamic flow and the motion of particles under the influence of a magnetic field ($B_r = 2T$). The computational simulations demonstrate that the greatest particle capture efficiency result for particle diameters within the micron range, specifically 4 μm in regions where flow separation and vortices are at a minimum. It was also determined that the capture efficiency of particles decreases substantially with particle diameter, especially in the superparamagnetic regime. It is also worth noting that several simplifications have been introduced in the computational simulations involving the vessel geometry, boundary conditions, and particle modeling.

Some of these simplifications include restructuring portions of the arterial model that promote meshing irregularities, modelling the vessel as a rigid wall vessel, implementing a velocity inlet waveform that does not match the true waveform of the subject being studied, and not modelling the drug thickness on particles. It is unlikely that improvements in these simplifications will severely alter the capture efficiency results significantly. Perhaps the most significant simplification was made by evaluating the drag force for superparamagnetic particles *via* Stokes expression, using the Carreau non-Newtonian fluid viscosity model. The Carreau fluid viscosity model projects a significantly higher viscosity than the actual viscosity of blood plasma. In this case, small particles within the superparamagnetic regime may tend to move along stream traces in the blood plasma without colliding with blood constituents, therefore experiencing a drag force proportional to the viscosity of the blood plasma. The viscous drag experienced by particles of the order of or smaller than the blood cells, as used in the present work, may therefore be much smaller than that which is presently used by considering the Carreau viscosity model. This could significantly change the outcome of capture efficiency for superparamagnetic particles in computational simulations such as those presented in the present work. The obtained capture efficiency results for the superparamagnetic could be significantly underestimated.

In addition, the authors would like to mention that an alternative approach for increasing capture efficiency of smaller particles in larger arteries may be done potentially by modeling a magnetized cardiovascular stent in the diseased sections as opposed to targeting particles in diseased sections of the artery during pre-stenting. In this case, the magnetized stents could potentially amplify the magnetic field gradient and increase particle capture of superparamagnetic particles. Future studies should explore experimentally and numerically, the effect of a secondary magnetic field produced by a magnetized stent on capture efficiency. Computational simulations such as those discussed in the present work make it possible to study the feasibility and practicality of MDT *a prior* to clinical trials. Furthermore, computational simulations are useful for investigating the influence of various factors independently and for optimization. The simulations results presented in the present work have shown to yield favorable capture efficiencies for micron range particles and a potential for enhancing capture efficiency of superparamagnetic particles in smaller arteries and/or using magnetized implants such as cardiovascular stents. The present work presents results for justifying further investigation of MDT.

ACKNOWLEDGMENTS

The authors would like to acknowledge Dr. Moloy Banerjee from the Future Institute of Engineering and Management Department of Mechanical Engineering in Kolkata India. Dr. Banerjee provided a great deal of insight and advice on developing the user defined function used in this work to describe the magnetic field produced by the external cylindrical coil. The authors would also like to acknowledge the University of North Carolina at Charlotte (UNC-C) Faculty Research Grant (FRG) and the Wells Fargo Faculty Grant through the Charlotte Research Institute (CRI) which funded this work. Lastly, the authors would like to acknowledge the North Carolina Space Grant Graduate fellowship through the National Aeronautics and Space Administration (NASA) which provided summer funding for the graduate student (Ashley Ciero) to work on this research.

CONFLICT OF INTERESTS

The authors of this work declare no conflict of interests.

HUMAN STUDIES/INFORMED CONSENT

No human studies were carried out by the authors for this article.

ANIMAL STUDIES

No animal studies were carried out by the authors for this article.

REFERENCES

[1]Al-Jamal, T., J. Bai, J. Wang, *et al*. Magnetic drug targeting: preclinical in vivo studies, mathematical modeling, and extrapolation to humans. *Nano Lett*. 16:5652–5660, 2016.

[2]Aviles, M. O., H. Chen, A. D. Ebner, *et al*. In vitro study of ferromagnetic stents for implant assisted-magnetic drug targeting. *J. Magn. Mater*. 311(1):306–311, 2007.

[3]Boghi, A., F. Russo, and F. Gori. Numerical simulation of magnetic nano drug targeting in a patient-specific coeliac trunk. *J. Magn. Magn. Mater*. 437:86–97, 2017.

[4]Bose, S., and M. Banerjee. Magnetic particle capture for biomagnetic fluid flow in stenosed aortic bifurcation considering particle-fluid coupling. *J. Magn. Magn. Mater*. 385:32–46, 2015.

[5]Bose, S., A. Datta, R. Ganguly, and M. Banerjee. Lagrangian magnetic particle tracking through stenosed artery under pulsatile flow condition. *J. Nano. Eng. Med*. 4(3):1–10, 2014.

[6]Buchmann, A. C., M. C. Jeremy, and J. Soria. Tomographic particle image velocimetry investigation of the flow in a modeled human carotid artery bifurcation. *Exp. Fluids* 50(4):1131–1151, 2011.

[7]Chen, H., A. F. Ebner, A. B. Rosengart, *et al*. Analysis of magnetic drug carrier particle capture by a magnetizable intravascular stent: 1. parametric study with single wire correlation. *J. Magn. Magn. Mater*. 284:181–194, 2004.

[8]Cheung, S. C., K. K. Wong, G. H. Yeoh, *et al*. Experimental and numerical study on the hemodynamics of stenosed carotid bifurcation. *Australas. Phys. Eng. Sci. Med*. 33(4):319–328, 2011.

[9]Chorny, M., I. Fishbein, I. Alferiev, and R. J. Levy. Magnetically responsive biodegradable nanoparticles enhanced adenoviral gene transfer in cultured smooth muscle and endothelial cells. *Mol. Pharm*. 6(5):1380–1387, 2009.

[10]Chorny, M., I. Fishbein, S. Forbes, and I. Alferiev. Magnetic nanoparticles for targeted vascular delivery. *IUBMB Life* 62(8):613–620, 2011.

[11]Chorny, M. F., I. Fishbein, B. B. Yellen, *et al*. Targeting stents with local delivery of paclitaxel-loaded magnetic nanoparticles using uniform fields. *Proc. Natl. Acad. Sci. USA* 107(18):8346–8351, 2010.

[12]Chorny, M., B. Polyak, I. S. Alferiev, *et al*. Magnetically driven plasmid DNA delivery with biodegradable polymeric nanoparticles. *FASEB J*. 21(10):2510–2519, 2007.

[13]Diaconu, A., A. P. Chiriac, N. Tudorachi, *et al*. Investigation concerning the possibilities for the deposition of magnetic nanoparticles onto a metallic stent. *Rev. Roum. Chim*. 62(8–9):677–685, 2017.

[14]Forbes, Z. G., B. B. Yellen, D. S. Halverson, *et al*. Validation of high gradient magnetic field based drug delivery to magnetizable implants under flow. *IEEE Trans. Bio-Med. Eng*. 55(2):643–649, 2008.

[15]Furlani, E. J., and E. P. Furlani. A model for predicting magnetic targeting of multifunctional particles in the microvasculature. *J. Magn. Magn. Mater*. 312:187–193, 2007.

[16]Furlani, E. P., and K. C. Ng. Analytical model of magnetic nanoparticle transport and capture in the microvasculature. *Phys. Rev. E* 73:061919, 2006.

[17]Gay, M., and L. Zhang. Numerical studies of blood flow in healthy, stenosed, and stented carotid arteries. *Int. J. Numer. Method Fluid* 61(4):453–472, 2009.

[18]Gharahi, H., B. Zambrano, D. Zhu, *et al*. Computational fluid dynamic simulation of human carotid artery bifurcation based on anatomy and volumetric blood flow rate measured with magnetic resonance imaging. *Int. J. Adv. Eng. Sci*. 8(1):40–60, 2016.

[19]Goya, G. F., V. Grazu, and M. R. Ibarra. Magnetic nanoparticles for cancer therapy. *Curr. Nanosci*. 4(1):1–16, 2008.

[20]Grief, A., and G. Richardson. Mathematical modelling of magnetically targeted drug delivery. *J. Magn. Magn. Mater*. 293(1):455–463, 2005.

[21]Haider, A., and O. Levenspiel. Drag coefficient and terminal velocity of spherical and nonspherical particles. *Powder Technol*. 58:63–70, 1989.

[22]Haverkort, J. W., K. Kenjeres, and C. R. Kleijn. Computational simulations of magnetic particle capture in arterial flows. *Ann. Biomed. Eng*. 37:2436–2448, 2009.

[23]Hewlin, R. Transient Cardiovascular Hemodynamics in a Patient-Specific Arterial System. New York: ProQuest Dissertation Publishing, 2015.
[24]Hewlin, R., and J. Kizito. Comparison of carotid bifurcation hemodynamics in patient-specific geometries at rest and during exercise. ASME Fluids Engineering Division Summer Meeting, vol. 82(74), 2013.
[25]Iacob, G., O. Rotariu, N. J. C. Strachan, and U. O. Hafeli. Magnetizable needles and wires-modeling an efficieny way to target magnetic microspheres in vivo. *Biorheology* 41:599–612, 2004.
[26]Liu, Y., J. Tan, A. Thomas, *et al*. The shape of things to come: importance of design in nanotechnology for drug delivery. *Ther. Deliv*. 3(2):181–194, 2012.
[27]Lubbe, A. S., C. Bergemann, H. Riess, *et al*. Clinical experiences with magnetic drug targeting: a phase I study with 4′-epidoxorubicin in 14 patients with advanced solid tumors. *Cancer Res*. 15(56):4686–4693, 1996.
[28]Lunnoo, T., and T. Puangmali. Capture efficiency of biocompatible magnetic nanoparticles in arterial flow: a computer simulation for magnetic drug targeting. *Nanoscale Res. Lett*. 10(426):1–11, 2015.
[29]Morsi, S. A., and A. J. Alexander. An investigation of particle trajectories in two-phase flow systems. *J. Fluid Mech*. 55(2):193–208, 1972.
[30]Ning, P., C. Lanlan, K. Yang, *et al*. Uniform magnetic targeting of magnetic particles attracted by a new ferromagnetic biological patch. *Bioelectromagnetics* 39(2):98–107, 2018.
[31]Ounis, H., G. Ahmadi, and J. B. McLaughlin. Brownian diffusion of submicrometer particles in viscous sublayer. *J. Colloid Interface Sci* 143(1):266–277, 1991.
[32]Polyak, B., I. Fishbein, M. Chorny, *et al*. High field gradient targeting of magnetic nanoparticle-loaded endothelial cells to the surface of steel stents. *Proc. Natl. Acad. Sci. USA* 105(2):698–703, 2008.
[33]Russo, F., A. Boghi, and F. Gori. Numerical simulation of magnetic nano drug targeting in patient-specific lower respiratory tact. *J. Magn. Magn. Mater*. 451:554–564, 2018.
[34]Shubayev, V. I., T. R. Pisanic, and S. Jin. Magnetic nanoparticles for theragnostics. *Adv. Drug Deliv. Rev*. 61:467–477, 2009.
[35]Sui, B., P. Gao, Y. Lin, *et al*. Assessment of wall shear stress in the common carotid artery of healthy subjects using 3.0-tesla magnetic resonance. *Acta. Radiol*. 49(4):442–449, 2008.
[36]Takayasu, M., R. Gerber, and F. J. Friedlaender. Magnetic separation of submicron particles. *IEEE Trans. Magn*. 19(5):2112–2114, 1983.
[37]Tefft, B. J., S. Uthamaraj, J. J. Harburn, *et al*. Magnetizable stent-grafts enable endothelial cell capture. *J. Magn. Magn. Mater*. 427:100–104, 2017.
[38]Tzirtzolakis, E. E., and V. C. Loukopoulos. Biofluid flow in a channel under the action of a uniform localized magnetic field. *Comp. Mech*. 36(5):360–374, 2005.
[39]Vetel, J., A. Garon, and S. Pelletier. Lagrangian coherent structures in the human carotid artery bifurcation. *Exp. Fluids* 46(6):1067–1079, 2009.
[40]Wong, B. S., Y. G. Low, W. Xin, et al. 3D finite element simulation of magnetic particle inspection. Sustainable Utilization and Development in Engineering and Technology (STUDENT) 2010 IEEE Conference on 20–21 Nov, 2010, p. 50–55.
[41]Xiao, L., S. Beibei, Z. Huilin, *et al*. Retrospective study of hemodynamic changes before and after carotid stenosis formation by vessel surface repairing. *Nature* 5493:1–8, 2018.